

## Article

# Investigation of the Effect of Magnetic Field and Propellant on Hall Thruster's Stability via a 0D Model

Luca Leporini <sup>1,\*</sup> , Ferhat Yaman <sup>1</sup> , Tommaso Andreussi <sup>1,2</sup> and Vittorio Giannetti <sup>1,2</sup>

<sup>1</sup> Department of Civil and Industrial Engineering, University of Pisa, 56122 Pisa, Italy; f.yaman@studenti.unipi.it (F.Y.); tommaso.andreussi@santannapisa.it (T.A.); vittorio.giannetti@santannapisa.it (V.G.)

<sup>2</sup> Institute of Mechanical Intelligence, Sant'Anna School of Advanced Studies, 56010 Pisa, Italy

\* Correspondence: luca.leporini@phd.unipi.it

**Abstract:** Hall thrusters are plasma-based devices that have established themselves as one of the most attractive and mature electric propulsion technologies for space applications. These devices often operate in a regime characterized by low frequency, large amplitude oscillations of the discharge current, which is commonly referred to as the 'breathing mode'. The intensity of these oscillations depends on the thruster's design and operating conditions and can reach values of the order of the average discharge current, posing issues for the thruster's performance and for coupling with the driving electronics. A 0D model of the thruster discharge was developed to investigate the core physical mechanisms leading to the onset and sustenance of the breathing mode. The model was found to be capable of reproducing oscillations with characteristics in line with those observed in the breathing mode. In this work, we extend the use of the 0D model to investigate the effect of the magnetic field intensity and of different propellants on the system stability.

**Keywords:** electric propulsion; Hall thruster; plasma oscillations; breathing mode; ionization instability; alternative propellants



**Citation:** Leporini, L.; Yaman, F.; Andreussi, T.; Giannetti, V. Investigation of the Effect of Magnetic Field and Propellant on Hall Thruster's Stability via a 0D Model. *Aerospace* **2024**, *11*, 227. <https://doi.org/10.3390/aerospace11030227>

Academic Editor: Jae Hyun Park

Received: 8 February 2024

Revised: 8 March 2024

Accepted: 13 March 2024

Published: 14 March 2024



**Copyright:** © 2024 by the authors. Licensee MDPI, Basel, Switzerland. This article is an open access article distributed under the terms and conditions of the Creative Commons Attribution (CC BY) license (<https://creativecommons.org/licenses/by/4.0/>).

## 1. Introduction

Hall thrusters are plasma-based electric propulsion devices that have been employed for a wide range of space applications, from satellite orbit raising and station keeping to deep space missions. An overview of these devices can be found, for instance, in [1–3].

Hall thrusters are mainly composed of a ceramic annular discharge channel, a magnetic circuit that generates and shapes the magnetic field, which has a predominant radial component and peaks in the vicinity of the channel exit, and two electrodes, an anode, and a cathode. The anode, which also serves as a gas distributor, is placed at the bottom of the channel and is biased a few hundred volts above the external cathode. During operation, a flux of propellant gas is injected into the discharge chamber through the anode, while the electrons emitted by the cathode are attracted toward the anode and energized due to the increasing electric potential. In the region where the radial component of the magnetic field is large enough, the crossed electric and magnetic fields force the electrons to perform an  $E \times B$  drift in the azimuthal direction. When the neutral flux reaches the region of high electron density, it becomes ionized quickly by electron impact, generating plasma. If the magnetic field is properly tailored, the ions thus generated are not forced to drift azimuthally (due to their large inertia compared to the electrons) and are accelerated outside of the channel by the axial electric field, generating the thrust. The new electrons generated by the ionization of the propellant join the primary population coming from the cathode and drift through successive collisions until they are collected by the anode. The ion beam is then neutralized by part of the electrons emitted by the cathode, preserving the overall charge neutrality of the system.

The use of crossed electric and magnetic fields in these devices allows for the effective ionization and acceleration of the propellant gas but is also the source of rich and complex plasma physics that leads to the formation of a variety of unsteady modes [4]. The characteristics of these instabilities, which span a wide range of length and time scales, depend on the thruster's magnetic field intensity and topology, geometry, and operating conditions, defined in terms of a propellant mass flow rate and discharge voltage.

One of the most prominent modes, known as the breathing mode, is recognized as a relatively low frequency (5–30 kHz), large amplitude (of the order of  $\sim 100\%$  of the DC value) oscillation of the discharge current, which is generated by a correspondent longitudinal fluctuation of the plasma parameters in the thruster's channel and near plume. These fluctuations, when particularly violent, can have a detrimental impact on the thruster's performance and cause issues for the coupling with the driving electronics. Thus, their onset is largely avoided, typically by limiting the operating envelope of the thruster. This has justified extensive research efforts in recent decades that encompassed both experimental and numerical approaches.

From an experimental perspective, since the 1970s [5], several works aimed at characterizing the discharge oscillations for different thrusters and operating conditions. A relevant example is the work of Sekerak et al. [6,7], who identified two different operating regimes for a fixed operating point, depending on the magnitude of the magnetic field: a more quiescent "local" mode at high magnetic field intensities and a "global" mode at low intensities, characterized by a sudden increase of both the DC and AC components of the discharge current. The transition was observed to shift towards higher magnetic fields when the voltage and/or the mass flow rate were increased. More recently, Giannetti et al. [8] presented the results of the processing of a large amount of thrust and current trace measurements to derive general data-driven scaling laws for current oscillations and thruster performance when the channel geometry and operating conditions of the thruster are varied. Different types of intrusive [9–11] and nonintrusive [12–15] diagnostic have also been used to characterize the longitudinal plasma dynamics in the channel and near plume during the breathing mode cycles.

On the numerical side, the pioneering research of Fife et al. [16] and Boeuf et al. [17] brought to light the nature of the breathing mode as an ionization instability, characterized by the cyclic ionization and depletion of the propellant gas in the chamber, followed by the plasma expulsion through the electrostatic acceleration of the ions and the subsequent replenishment of the chamber from the propellant flux incoming from the anode. Since then, a variety of numerical models, particularly 0D [18–20] and 1D [21–27], have been developed with the ultimate goal of increasing our understanding of the breathing mode. However, a comprehensive and unanimously accepted picture of the mechanism responsible for the onset and growth of this instability is still missing in the literature, limiting our ability to predict and mitigate it across different geometries, propellants, and operating conditions.

In Ref. [25], a series of numerical experiments performed with a 1D model of the discharge (which was calibrated against the experimental discharge current signal of a 5 kW-class Hall thruster operating with xenon in global mode [28]) allowed the authors to identify the core physical mechanism behind the growth of the observed breathing oscillations. The analysis orbited around the identification of the base state, i.e., the unsteady equilibrium solution upon which the breathing mode develops. Results showed that a linear dependence for oscillations of electron mobility with variations in neutral density is necessary and sufficient for triggering the instability in the proposed model, by inducing fluctuations in the electric field in phase opposition. The electric field, in turn, makes the ion velocity fluctuate in phase with it, favoring the accumulation and subsequent convection of plasma, thus fueling the instability. In this process, electron temperature fluctuations only play a secondary role and are not fundamental for the growth of the oscillations. Moreover, the proportionality coefficient with which variations in neutral density are reflected in changes in electron mobility (which was referred to as the "rigidity"

coefficient) was observed to play a fundamental role in the system stability, controlling the rate at which the oscillations grow or are damped.

Based on these results, an original 0D formulation was proposed in [20] to investigate the same thruster geometry and operating conditions. The 0D model, which basically consisted of a modified predator–prey formulation in which the ions are convected outside with a velocity that fluctuates in phase opposition with the neutral density, was shown to undergo a stability transition in correspondence with a threshold value of the rigidity coefficient, exhibiting self-sustained oscillations with the typical characteristics of the breathing mode, even when the electron temperature was kept constant. In order to investigate the stability of the model in a general sense, the electron mobility at the base state and the rigidity coefficient were treated as free parameters throughout the analysis, neglecting their dependence on the magnetic field strength and the plasma parameters.

In this paper, the 0D model presented in [20] is developed to provide further demonstration of the capabilities of the formulation to reproduce the salient features of the breathing mode, as well as to investigate general behaviors and qualitative trends concerning the effect of different operating parameters on the thruster stability. First, we focus on the intensity of the magnetic field, which is known to strongly affect the onset of the breathing mode [6,7]. In order to carry this out, we expand the model equations with the introduction of a closure model for the variations of the electron mobility and rigidity coefficient with the plasma parameters and the magnetic field intensity. Then, we investigate the sensitivity to the use of different propellants, namely krypton and argon, by introducing in the model the corresponding reaction rates. The choice of analyzing these propellants is motivated by the following reasons: first, they are gaining momentum as valid alternatives to xenon, which is extremely expensive and difficult to procure; second, they cover a wide range of atomic masses, which results in very different neutral and ion inertia; and third, they are noble gases, allowing us to avoid further complications due to different chemical reactions that would necessarily have to be considered, for instance, in the case of iodine. Furthermore, there is little information in the literature regarding thruster stability with alternative propellants. Finally, we perform a parametric analysis to investigate the effect of the anode temperature, which can provide useful information about the thermal transient after the thruster ignition.

The geometry and operating conditions under consideration are consistent with those described in earlier publications [20,28]. This allows us to perform a direct comparison between the 0D model and the higher-order experimentally calibrated 1D solution and to tune the 0D model accordingly. The stability properties of the model for varying operating parameters are characterized using a linear stability analysis. Given the lack of a dedicated set of experimental data to perform a direct comparison, the observed stability trends when moving away from the reference experimental calibration point are only discussed in the context of literature experimental observations. Ultimately, this work presents a numerical framework that demonstrates the capabilities of 0D formulations to reproduce the breathing mode in Hall thrusters and provides insight into the sensitivity of the thruster stability to magnetic field strength and different propellants.

The paper is organized as follows: In Section 2, the equations and assumptions of the numerical model are briefly revised and expanded to introduce a direct dependence on the magnetic field intensity. In Section 3, the results of the stability analysis for varying magnetic field strength are shown and discussed; the effect of different propellants (namely xenon, krypton, and argon) and anode temperature on the thruster's stability is also investigated. Finally, Section 4 summarizes the conclusions of the present work.

## 2. Method

In this section, we briefly review the main model assumptions and equations. For a more formal derivation, the reader is kindly referred to [20].

The 0D formulation was derived from the 1D model detailed in [28] that was calibrated on the experimental discharge current trace of a 5 kW Hall thruster operating with xenon

and exhibiting large breathing mode oscillations. The calibrated 1D model was shown to be effective in reproducing the characteristic features of the breathing mode, with the simulated discharge dynamics exhibiting remarkable agreement with the experimental reference data. The main 1D model assumptions and parameters were retained in the derivation of the 0D formulation [20].

In particular, the model considers three species, namely neutrals, electrons, and singly charged ions. Plasma is assumed to be quasineutral, thus the electron and ion densities are the same. Neutrals have constant and uniform velocity, ions are cold and unmagnetized, and the electron inertia is neglected. The neutral and plasma dynamics are assumed to be purely axial, while the radial diffusion and plasma–wall interactions are taken into account through appropriate source/sink terms. The 0D equations were derived by integrating the correspondent 1D equations and averaging over the selected control volume, which comprises the whole thruster discharge chamber, thus extending over a length  $L$  enclosed between the anode (A) and the channel exit section (E) of the thruster and the lateral walls. A schematic representation of the control volume is shown in Figure 1.

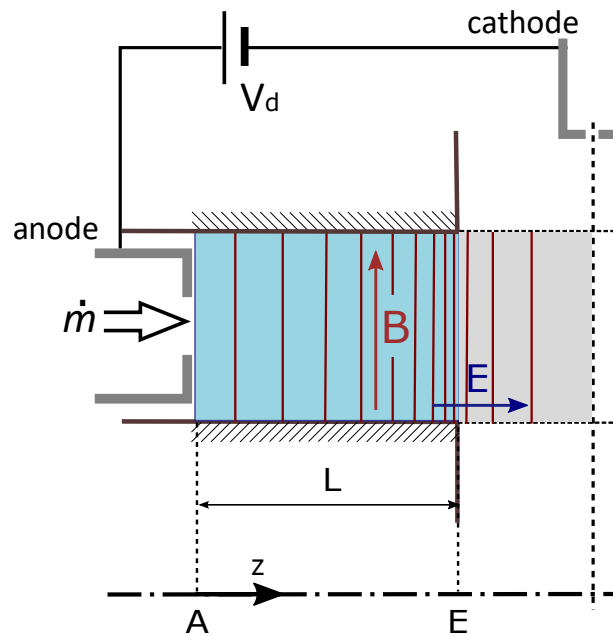


Figure 1. Schematic representation of the control volume, highlighted in blue.

Several assumptions were then made to express the integral as analytical functions of the averaged plasma parameters. In particular, neutral ( $n_n$ ) and plasma ( $n$ ) densities, electron temperature ( $T_e$ ), and electron mobility ( $\mu$ ) are considered to be uniform inside the control volume, while electron ( $u_e$ ) and ion ( $u_i$ ) velocities are assumed to vary linearly. The neutral velocity ( $u_n$ ) is constant and uniform. Moreover, the current is assumed to be carried only by electrons at the anode and only by ions at the channel exit section. As a consequence,  $u_{iA} = u_{eE} = 0$ ,  $u_{eA} = -u_{iE} = -2\bar{u}_i$  and  $\bar{u}_e = -\bar{u}_i$ , where the subscripts A and E indicate the anode and channel exit sections, and the over-bar represents the mean value operator in the considered control volume. The resulting set of equations is as follows:

$$\frac{d\bar{n}_n}{dt} + \frac{u_n}{L}(\bar{n}_n - n_{nA}) - 2\alpha \frac{\bar{n}\bar{u}_B}{\Delta R} = -\bar{n}_n\bar{n}\bar{k}_I, \tag{1}$$

$$\frac{d\bar{n}}{dt} + \frac{2\bar{n}\bar{u}_i}{L} + 2\alpha \frac{\bar{n}\bar{u}_B}{\Delta R} = \bar{n}_n\bar{n}\bar{k}_I, \tag{2}$$

$$\frac{d}{dt}(\bar{n}\bar{u}_i) + \frac{4\bar{n}\bar{u}_i^2}{L} + 2\alpha \frac{\bar{n}\bar{u}_B\bar{u}_i}{\Delta R} = \frac{e}{m_i}\bar{n}\bar{E}, \tag{3}$$

$$\frac{d}{dt} \left( \frac{3}{2} \bar{n} k_B \bar{T}_e \right) = \frac{e}{m_i} \bar{n} \bar{E} \bar{u}_i - \bar{n} \bar{n}_n \bar{K} - \bar{n} \bar{W}. \quad (4)$$

In the previous equations,  $t$  denotes the time,  $e$  is the elementary charge,  $m_i$  is the mass of the propellant atoms, respectively,  $k_B$  is the Boltzmann constant,  $\Delta R$  is the width of the discharge channel,  $u_B$  is the Bohm velocity at the lateral walls,  $n_{nA}$  is the neutral density at the anode section,  $E$  is the electric field,  $W$  represents the electron power loss at the lateral walls, and  $\alpha$  is a coefficient modulating the plasma wall interactions, which was introduced in [28] as a calibrating parameter of the model to address the unresolved radial variations in plasma profiles and the uncertainties in the semi-empirical description of the plasma–wall interaction. Coefficients  $\bar{k}_I$  and  $\bar{K}$  are the (averaged) ionization rate and collisional energy loss coefficients, respectively. Since the electron temperature is assumed constant throughout the channel, these quantities can be expressed as functions of the averaged electron temperature,

$$\bar{k}_I = k_I(\bar{T}_e), \quad (5)$$

$$\bar{K} = K(\bar{T}_e), \quad (6)$$

and computed using the LXCat database [29] and the Bolsig+ solver [30]. The quantities accounting for the plasma–wall interaction are described following the classical formulation of Hobbs and Wesson [31] for a 1D planar sheath in the presence of secondary electron emission:

$$\bar{u}_B = \sqrt{\frac{k_B \bar{T}_e}{m_i}}, \quad (7)$$

$$\bar{W} = \alpha \frac{\bar{u}_B}{1 - \sigma} (2k_B \bar{T}_e + (1 - \sigma)e\bar{\phi}_w) \frac{2}{\Delta R}, \quad (8)$$

$$\bar{\phi}_w = \frac{k_B \bar{T}_e}{e} \ln \left[ (1 - \sigma) \sqrt{\frac{m_i}{2\pi m_e}} \right], \quad (9)$$

where  $m_e$  is the electron mass,  $\phi_w$  is the sheath potential drop at the lateral walls, and  $\sigma$  is the effective secondary emission yield.

Equation (1) represents the conservation of neutral mass. The neutral density within the thruster channel, which is assumed to be uniform, is the result of a balance between different contributions: the flux going out from the channel exit, the propellant injected from the anode, the ion neutralization at the lateral walls (second, third, and fourth terms on the lhs, respectively), and the propellant ionization (on the rhs). The flux of neutrals coming from the anode is related to the operating condition of the thruster through the injected propellant mass flow rate as follows:

$$n_{nA} = \frac{\dot{m}}{m_i u_n A_{ch}}, \quad (10)$$

where  $\dot{m}$  and  $A_{ch}$  are the injected propellant mass flow rate and the channel area. The neutral velocity is related to the anode temperature  $T_A$ :

$$u_n = \sqrt{\frac{8k_B T_A}{\pi m_i}}. \quad (11)$$

The ion continuity equation (Equation (2)) is similar to the neutral mass balance, but we have used  $u_{iA} = 0$  and  $u_{iE} = 2\bar{u}_i$ . Moreover, the ion velocity is allowed to vary according to an appropriate momentum conservation equation (Equation (3)). In particular, the ion momentum is the result of a balance between the momentum lost through the boundaries of the control volume (second and third terms on the lhs of the equation) and the electrostatic acceleration.

Equation (4) represents the conservation of electron internal energy. Basically, Equation (4) states that part of the energy gained through resistive heating is spent to

ionize the propellant, while another part is lost at the lateral walls (convective and heat flux terms have been neglected).

Concerning the electric field, the 1D Ohm's law provides

$$E = -\frac{u_e}{\mu} - \frac{1}{e n_e} \frac{\partial p_e}{\partial z}, \quad (12)$$

where  $p_e$  is the electron pressure, and  $z$  is the axial coordinate. Within the assumptions previously made, the effect of the pressure gradient is neglected, while the electron mobility and velocity are uniform and linearly varying, respectively. Thus, the averaged electric field can be expressed as

$$\bar{E} = -\frac{\bar{u}_e}{\bar{\mu}} = \frac{\bar{u}_i}{\bar{\mu}}, \quad (13)$$

where we have used  $\bar{u}_e = -\bar{u}_i$ .

In [25], the authors showed that a linear dependence of the electron mobility on the neutral density is necessary and sufficient to trigger the breathing mode. In that paper, a simplified expression for  $\mu$  was derived by linearizing it around the base state while neglecting contributions of electron temperature variations, which were demonstrated to be of secondary importance for the onset and sustenance of the instability, obtaining

$$\mu \approx \mu_b + \gamma(n_n - n_{nb}), \quad (14)$$

where the subscript "b" denotes the base state, and the coefficient  $\gamma$  plays the role of a rigidity which linearly relates fluctuations in the neutral density to variations in the electron mobility. Basically, variations in neutral density induce fluctuations in the electric field in phase opposition through electron mobility. The electric field, in turn, acts on the ion dynamics, making the ion velocity fluctuate in phase with it. Compared to pure predator-prey dynamics, when the neutral density is high (and so is the ionization rate), the ion velocity is low, which favors the accumulation of plasma, making the subsequent neutral depletion more violent. The opposite happens in the other half of the cycle: when the neutral density is low (and so is the ionization rate), the ion velocity is high, and the plasma is quickly convected outside, favoring the subsequent accumulation of neutrals. This process strengthens the classical predator-prey dynamics, and if  $\gamma$  is sufficiently large, it can lead to the growth in fluctuations and the onset of instability.

Without altering this physical mechanism, which is believed to be the core of the onset of the breathing mode [25], the averaged electron mobility in the 0D formulation can then be expressed as follows:

$$\bar{\mu} = \bar{\mu}_b + \bar{\gamma}(\bar{n}_n - \bar{n}_{nb}). \quad (15)$$

The purpose of the analysis conducted in [20] with the presented model was to support the conclusion that the mechanism described above is sufficient to trigger the breathing mode in Hall thrusters. Thus, in order to study the system more generally,  $\bar{\mu}$  and  $\bar{\gamma}$  were considered as free parameters throughout the study, and the stability of the system was assessed for a plausible parameter space. However, as shown in [25], the electron mobility at the base state and the rigidity coefficient are, in principle, both functions of the radial magnetic field intensity along the thruster channel ( $B_r(z)$ ) and plasma quantities (neutral density and electron temperature) evaluated at the base state through the following relations:

$$\mu_b = \frac{e}{v_{eb} m_e} \frac{1}{1 + \left(\frac{\omega_e}{v_{eb}}\right)^2} = \mu_b(n_{nb}, T_{eb}, B_r) \quad (16)$$

$$\gamma = \frac{e}{m_e (v_{eb}^2 + \omega_e^2)} \left[ 1 - \frac{2v_{eb}^2}{(v_{eb}^2 + \omega_e^2)} \right] k_m = \gamma(n_{nb}, T_{eb}, B_r) \quad (17)$$

where  $\omega_e$  is the electron cyclotron frequency,  $\nu_e$  is the total electron scattering collision frequency, which is the sum of the classical ( $\nu_c$ ), wall ( $\nu_{ew}$ ), and anomalous ( $\nu_a$ ) collision frequencies, and  $k_m$  represents the reaction rate for momentum transfer collisions occurring between electrons and neutrals. We remind you here that, in principle,  $\mu$  would depend also on the plasma density through the elastic Coulomb collisions and, potentially, on the other plasma parameters through the anomalous collision frequency. Here, however, as well as in [25,28], we neglect the Coulomb scattering collisions, and we assume that  $\nu_a$  obeys a Bohm-like scaling, meaning that it is only proportional (through a coefficient  $\beta$ ) to the magnitude of the radial magnetic field through the electron cyclotron frequency and is therefore independent on time.

By maintaining the same functional relations, it is possible to incorporate the magnetic field intensity into the model by introducing corresponding closures for the averaged electron mobility and rigidity coefficient. In particular, based on Equations (16) and (17), we can define

$$\bar{\mu}_b = \overline{\mu(\bar{n}_{nb}, \bar{T}_{eb}, B_r)} \quad (18)$$

$$\bar{\gamma} = \overline{\gamma(\bar{n}_{nb}, \bar{T}_{eb}, B_r)}, \quad (19)$$

where  $B_r(z)$  is the radial magnetic field profile along the thruster channel, and the over-bars again indicate the spatial average within the thruster channel. This will enable us to examine how the thruster's stability is altered when the magnetic field intensity is varied over a plausible range, as well as to perform a more direct comparison among the propellants. In particular, it is possible to scale the field strength while maintaining the same shape by defining the profile as  $B_r(z) = \frac{B_{max}}{B_{0,max}} B_0(z)$ , where  $B_0(z)$  and  $B_{0,max}$  are the experimental magnetic field profile used in the calibrated 1D solution and its peak value, and  $B_{max}$  replaces  $\bar{\mu}_b$  and  $\bar{\gamma}$  as the input parameter of the model. In this way, the 0D formulation considers the variation in the radial magnetic field intensity along the thruster channel, even though the magnetic field gradient does not explicitly appear in the equations after averaging.

The stability properties of the model for varying magnetic field intensity are assessed by employing a linear stability analysis. This was carried out by linearizing the model numerically, as proposed in [32], and by coupling the linearized model with an eigenvalue solver based on Krylov methods.

More in detail, we can express system 1–4 as follows:

$$\frac{d\mathbf{u}}{dt} = R(\mathbf{u}) \quad (20)$$

where  $\mathbf{u} \in \mathfrak{R}^n$  is the vector of variables, and  $R$  represents the discrete residuals. If  $\mathbf{u}^k$  is the vector of variables at the time  $t^k$ , the numerical scheme derived upon time discretization of system 20 allows the computation of  $\mathbf{u}^{k+1}$ , where  $t^{k+1} = t^k + \Delta t$ .

The steady-state solution of 20, which we will refer to also as the “base-state”, can be defined as the vector  $\mathbf{u}_b$  such that

$$R(\mathbf{u}_b) = 0. \quad (21)$$

The stability of the base state is then investigated by a numerical stability analysis. In particular, the linearized dynamics of a generic disturbance, which is at the basis of the linear stability analysis, is approximated numerically as follows.

First, we express the generic perturbation as  $\epsilon \mathbf{u}_p$ , with  $\epsilon \ll 1$ , such that

$$\mathbf{u}^k = \mathbf{u}_b + \epsilon \mathbf{u}_p^k, \quad (22)$$

$$\mathbf{u}^{k+1} = \mathbf{u}_b + \epsilon \mathbf{u}_p^{k+1}. \quad (23)$$

Thus, given  $\mathbf{u}_p^k$ , it is possible to define an operator  $N$  such that  $\mathbf{u}_p^{k+1} = N(\mathbf{u}_p^k)$  according to the following logical scheme:

1. Define  $\mathbf{u}^k = \mathbf{u}_b + \epsilon \mathbf{u}_p^k$ ;
2. Compute  $\mathbf{u}^{k+1}$  with the numerical scheme obtained from the time discretization of system 20;
3. Compute  $\mathbf{u}_p^{k+1} = \frac{\mathbf{u}^{k+1} - \mathbf{u}_b}{\epsilon}$

If  $\epsilon$  and  $\Delta t$  are sufficiently small,  $N$  can be approximated with a linear operator, with the corresponding associated matrix  $\mathbf{L}$  such that

$$\mathbf{u}_p^{k+1} = \mathbf{L} \mathbf{u}_p^k. \quad (24)$$

If we consider a perturbation in the form of  $\mathbf{u}_p = \hat{\mathbf{u}}_p e^{\lambda t}$ , where  $\hat{\mathbf{u}}_p$  is its spatial form and  $\lambda \in \mathbb{C}$ , then

$$\mathbf{u}_p^{k+1} = e^{\lambda \Delta t} \mathbf{u}_p^k. \quad (25)$$

Combining 24 and 25, it follows that  $\hat{\mathbf{u}}_p$  shall be an eigenvector of  $\mathbf{L}$ , i.e.,

$$\mathbf{L} \hat{\mathbf{u}}_p = \sigma \hat{\mathbf{u}}_p \quad (26)$$

with  $\sigma$  being its corresponding eigenvalue. Therefore, it is possible to relate the eigenvalues of  $\mathbf{L}$  with  $\lambda$  through

$$\lambda = \frac{1}{\Delta t} \ln \sigma. \quad (27)$$

The real and imaginary parts of  $\lambda$  correspond to the growth rate and frequency of the corresponding eigenmode, respectively. Thus, system 1–4 will be unstable if  $\Re(\lambda) > 0$  for at least one of the eigenvalues  $\sigma$  of  $\mathbf{L}$ . In particular, the dominant mode is defined as the mode with the largest real part.

The investigation is conducted on the same thruster's geometry ( $L$  and  $\Delta R$ ) and operating condition (discharge voltage  $V_d = 300$  V, xenon mass flow rate  $\dot{m} = 8$  mg/s, and reference magnetic field profile  $B_0$ ) of the calibrated 1D simulation [28]. In particular, the thruster is a 5 kW class device, and the operating condition is characterized by a well-developed breathing mode, with a frequency of approximately 25 kHz and an average discharge current of about 8.6 A. This particular configuration was extensively investigated both experimentally [11] and numerically [28], thus representing an optimal reference for the following analysis.

We highlight here that values of the calibrating parameters employed in the 1D formulation, namely, the neutral velocity ( $u_n$ ), the parameter modulating the plasma–wall interaction ( $\alpha$ ), and the scaling coefficient of the Bohm-like anomalous collision frequency ( $\beta$ ), are kept constant throughout the entire analysis, independently of the simulated value of the magnetic field and propellant. In particular, we set  $u_n = 395$  m/s,  $\alpha = 0.115$ , and  $\beta = 0.075$ , which are the values resulting from the calibration process presented in [28] for the same thruster and operating condition.

### 3. Results

#### 3.1. Effect of Magnetic Field

The results of the linear stability analysis are presented in Figure 2, which shows the growth rate and frequency of the resulting dominant mode for a representative range of magnetic field intensities. Interestingly, the implementation of functional relations with magnetic field intensity consistently yields stable outcomes. However, it is possible to identify two distinct regimes: for low magnetic fields, the growth rate increases (i.e., the system tends to become less stable) when  $B_{max}$  is lowered; for large magnetic fields, instead, the contrary happens, i.e., the growth rate reaches a minimum beyond which it starts growing for increasing  $B_{max}$ . Concerning the frequency, the linear stability analysis yields values in the range of 5–30 kHz, which are in line with those typically observed for the breathing mode instability in Hall thrusters. Moreover, the frequency tends to

grow with  $B_{max}$ , in agreement with previous experimental observations [6,8,33,34] and higher-order simulations [23] carried out by different authors and with different thrusters.

The fact that the growth rate increases at low magnetic fields is promising and requires further investigation. In particular, the range of magnetic fields reported in Figure 2 is limited at the lower end because, below a certain value of  $B_{max}$ , the electron temperature becomes too low to sustain the plasma. Moreover, as suggested in Ref. [20], the magnetic field strength has two simultaneous effects on the model stability: on one side, a reduction in  $B_{max}$  leads to an increase in  $\bar{\gamma}$  that tends to destabilize the system; on the other hand, the lower the magnetic field strength, the higher the electron mobility, the higher the value of  $\bar{\gamma}$  that is required for the system to become unstable. Thus, one possible reason for the lack of unstable outcomes is that the model does not properly estimate the averaged plasma properties at the base state.

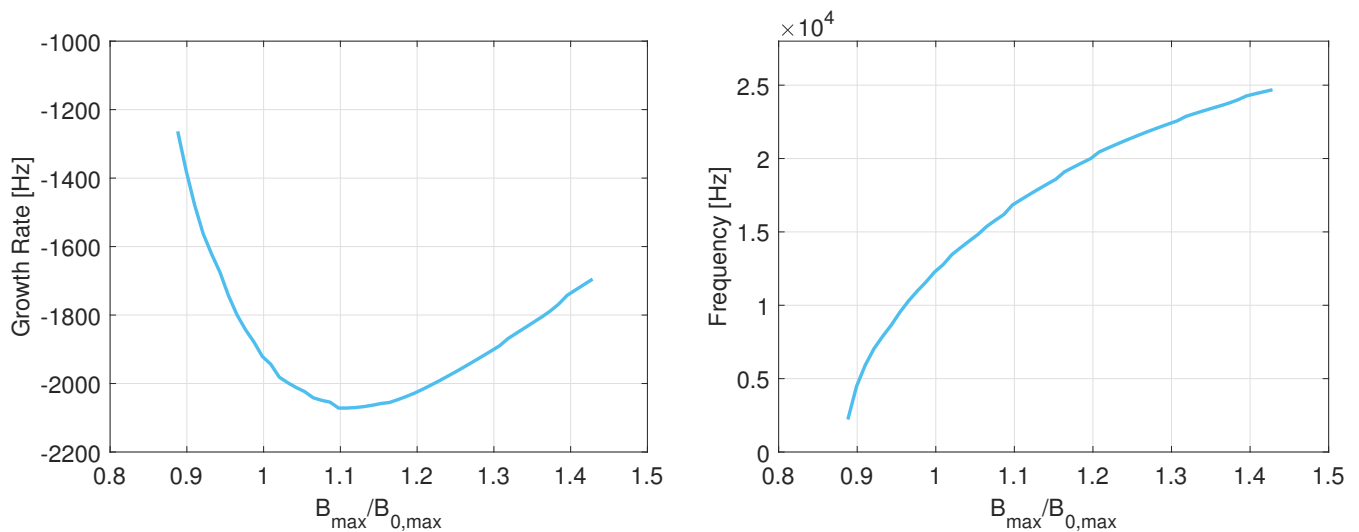


**Figure 2.** Result of the linear stability analysis: growth rate (left) and frequency (right) of the dominant mode for varying magnetic field intensity.

As mentioned in Section 2, the present 0D formulation has been derived by taking the average of the 1D equations of Giannetti et al. [28] within the thruster channel. Several assumptions have been made while passing from the integrated 1D equations to the 0D formulation. In particular, to express the integrals as analytical functions of the average properties, the various quantities have been assumed to have constant or linear profiles. In general, this is not true and the integrals of the products of the various quantities are not exactly equal to the product of the respective integrals. This leads to an error associated with each term of Equations (1)–(4). For instance, without losing generality, we can write

$$-\frac{1}{V} \int_V n_n n k_I dV = \overline{n_n n k_I} = c \bar{n}_n \bar{n} \bar{k}_I \quad (28)$$

where  $V$  is the control volume (corresponding in our case to the channel interior), and  $c$  is a coefficient quantifying the discrepancy between the two quantities, which can be evaluated for any specific condition. In our case, the reference condition is the base state associated with the experimentally calibrated 1D solution detailed in [25,28], from which the 0D model was derived. Equations (1)–(4) can thus be reformulated by introducing a correction coefficient  $c_n$  for every instance in which this approximation was carried out, and the value of these coefficients can be evaluated on the results of the experimentally calibrated 1D simulation base state to obtain a more representative 0D model of the discharge. It is important to note that the resulting coefficients are exact and representative of the experimentally calibrated higher-order simulation only for this specific reference condition. In principle, when investigating different operating points, the 1D model would need to be re-calibrated on new experimental data, and the coefficients would have to be re-computed

considering the new reference condition. Here, however, we compute the coefficients only once, and we extrapolate the results for other operating points from this calibrated reference state. In this way, we expect the tuned 0D model to be less representative far from the calibrated point. Nevertheless, the proposed model is not intended to provide predictive simulations but rather to be a useful numerical tool to investigate the main trends and the sensitivity of the stability of the discharge to the main thruster parameters in these regimes. The resulting equations are

$$\frac{d\bar{n}_n}{dt} + \frac{u_n}{L}(c_1\bar{n}_n - n_{nA}) - 2\alpha c_2 \frac{\bar{n}\bar{u}_B}{\Delta R} = -c_3\bar{n}_n\bar{n}\bar{k}_I, \quad (29)$$

$$\frac{d\bar{n}}{dt} + c_4 \frac{2\bar{n}\bar{u}_i}{L} + 2\alpha c_2 \frac{\bar{n}\bar{u}_B}{\Delta R} = c_3\bar{n}_n\bar{n}\bar{k}_I, \quad (30)$$

$$c_5 \frac{d}{dt}(\bar{n}\bar{u}_i) + c_6 \frac{4\bar{n}\bar{u}_i^2}{L} + 2\alpha c_7 \frac{\bar{n}\bar{u}_B\bar{u}_i}{\Delta R} = c_8 \frac{e}{m_i} \bar{n} \frac{\bar{u}_i}{\bar{\mu}}, \quad (31)$$

$$c_9 \frac{d}{dt} \left( \frac{3}{2} \bar{n} k_B \bar{T}_e \right) - c_{10} \frac{\frac{5}{2} \bar{n} k_B \bar{T}_e \bar{u}_i}{L} = c_{11} \frac{e}{m_i} \bar{n} \frac{\bar{u}_i^2}{\bar{\mu}} - c_{12} \bar{n} \bar{n}_n \bar{K} - c_{13} \bar{n} \bar{W}, \quad (32)$$

$$\bar{\mu} = \bar{\mu}_b + \overline{\gamma(n_n - n_{nb})} = c_{14} \overline{\mu(\bar{n}_{nb}, \bar{T}_{eb}, B_r)} + c_{15} c_{16} \overline{\gamma(\bar{n}_{nb}, \bar{T}_{eb}, B_r)} (\bar{n}_n - \bar{n}_{nb}). \quad (33)$$

Coefficients  $c_{14}$ ,  $c_{15}$  and  $c_{16}$  come from the following relations:

$$\bar{\mu}_b = \overline{\mu(n_{nb}, T_{eb}, B_r)} = c_{14} \overline{\mu(\bar{n}_{nb}, \bar{T}_{eb}, B_r)}, \quad (34)$$

$$\overline{\gamma(n_n - n_{nb})} = c_{15} \bar{\gamma}(\bar{n}_n - \bar{n}_{nb}), \quad (35)$$

and

$$\bar{\gamma} = \overline{\gamma(n_{nb}, T_{eb}, B_r)} = c_{16} \overline{\gamma(\bar{n}_{nb}, \bar{T}_{eb}, B_r)}. \quad (36)$$

The values of the coefficients computed from the experimentally calibrated 1D reference simulation are reported in Table 1. In the original 0D formulation, all the coefficients were implicitly set to be equal to 1, except for  $c_{10}$ , which was 0 since we were neglecting the convective transport of electron energy across the channel. Coefficient  $c_{10}$  is also the result of two contributions, the energy flux entering the channel from the exit section, and the one exiting the channel from the anode. The negative sign in the equation indicates that the former contribution is larger, and overall, convection introduces energy into the system. The terms with the higher associated error are mostly related to the neutral density at the channel exhaust ( $c_1$ ), ion acceleration ( $c_8$ ), electron energy absorption ( $c_{11}$ ), and energy losses to the walls ( $c_{13}$ ). Moreover, in the original formulation, the value of  $\bar{\gamma}$  was underestimated by a factor of 2 ( $c_{15}$ ).

**Table 1.** Values of the tuning coefficients of Equations (29)–(32) obtained by comparing the calibrated 1D solution to the correspondent 0D integrated equations.

Coefficient	Value	Coefficient	Value
$c_1$	0.17	$c_9$	0.9
$c_2$	0.94	$c_{10}$	0.25
$c_3$	0.73	$c_{11}$	2
$c_4$	0.65	$c_{12}$	0.73
$c_5$	0.72	$c_{13}$	2.74
$c_6$	0.75	$c_{14}$	1.3
$c_7$	0.8	$c_{15}$	2
$c_8$	1.86	$c_{16}$	0.88

It is possible now to repeat the linear stability analysis to verify whether the tuned model is capable of reproducing unstable solutions. The results are shown in Figure 3, where growth rate and frequency resulting from the linear stability analysis are again

reported as a function of the magnetic field intensity. Unlike the previous case, now the growth rate tends to rapidly decrease with the magnetic field intensity, which is an indication that stronger magnetic fields tend to suppress the breathing mode. Interestingly, the tuned 0D model identifies a minimum value of  $B_{max}$  below which the system becomes unstable. This behavior is coherent to the local-to-global mode transition that is typically observed in Hall thrusters operating at low magnetic fields, both in the experiments and in higher order simulations (see, for instance, [6–8,23]). Unfortunately, in the absence of dedicated experimental data for different magnetic field intensities, we could not perform a quantitative validation of these results. However, the fact that the same qualitative behavior was observed for different devices and operating conditions suggests that the observed trends are a general feature of the operation of these devices, which our simplified model was shown to be able to reproduce. Moreover, to the best of the authors' knowledge, this is the first time a transition in the operating mode of a Hall thruster at low magnetic fields has been predicted through a 0D model, which further supports the conclusion that the core physical mechanisms involved in the onset of the instability are correctly captured by the presented formulation. However, at the same  $B_{max}$  of the reference 1D simulation, which was characterized by a well-developed breathing mode, the tuned 0D model yields a comparable frequency but a negative growth rate. This could suggest that the onset and development of the breathing mode, even though they are regulated by the identified feedback mechanism, are a more localized phenomenon, which also depends on the local plasma parameters and gradients and on the interplay between the ionization and acceleration regions, which are overlapped in the 0D model.

Concerning the frequency, the tuned model yields results similar to the original one, with values in the order of 5–30 kHz and an increasing trend with respect to the magnetic field intensity.

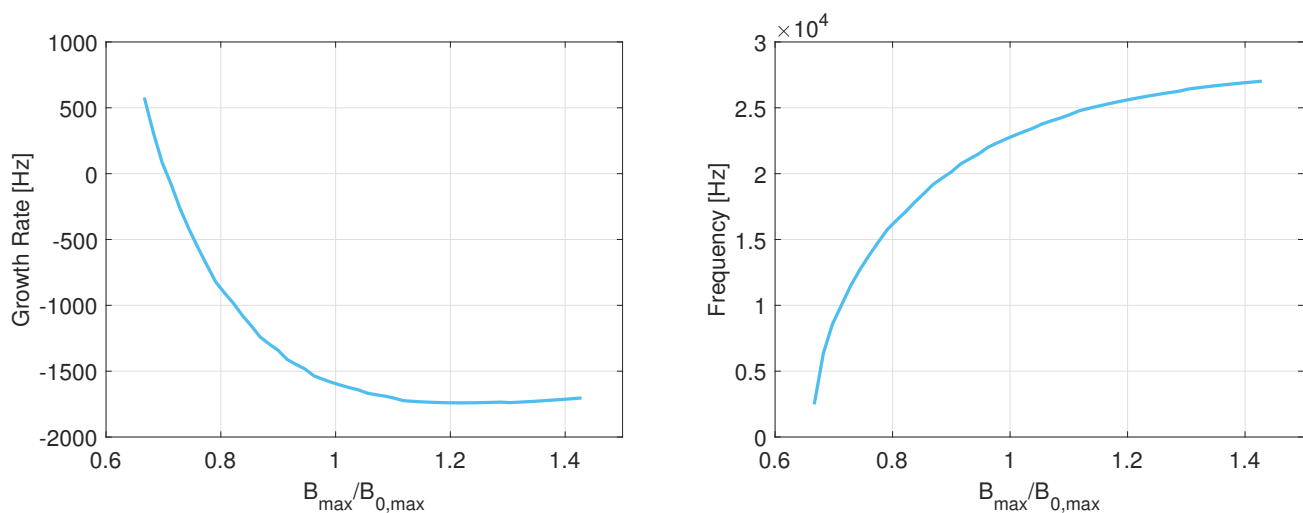


**Figure 3.** Result of the linear stability analysis applied to the tuned model: growth rate (left) and frequency (right) of the dominant mode for varying magnetic field intensity

Figure 4 reports the steady-state solution of the tuned system as a function of the magnetic field. The orders of magnitude of the resulting plasma quantities are in line with those typically observed in higher-order simulations. As expected, when the magnetic field is enhanced, the mobility monotonically decreases as a consequence of the stronger electron trapping in the channel. This determines an increase in the electric field and, in turn, in the ion velocity and electron temperature. We can also see that the temperature is more susceptible to variations in the magnetic field at lower values, while the curve flattens at larger  $B_{max}$ . A similar trend can be observed for the frequency of the instability (Figure 3). This behavior can be related to the predator–prey cycle which is the basis of the breathing mode dynamics: when the electron temperature in the ionization region

increases, the neutrals are consumed faster, lowering the time between the higher and the lower peaks of the oscillation.

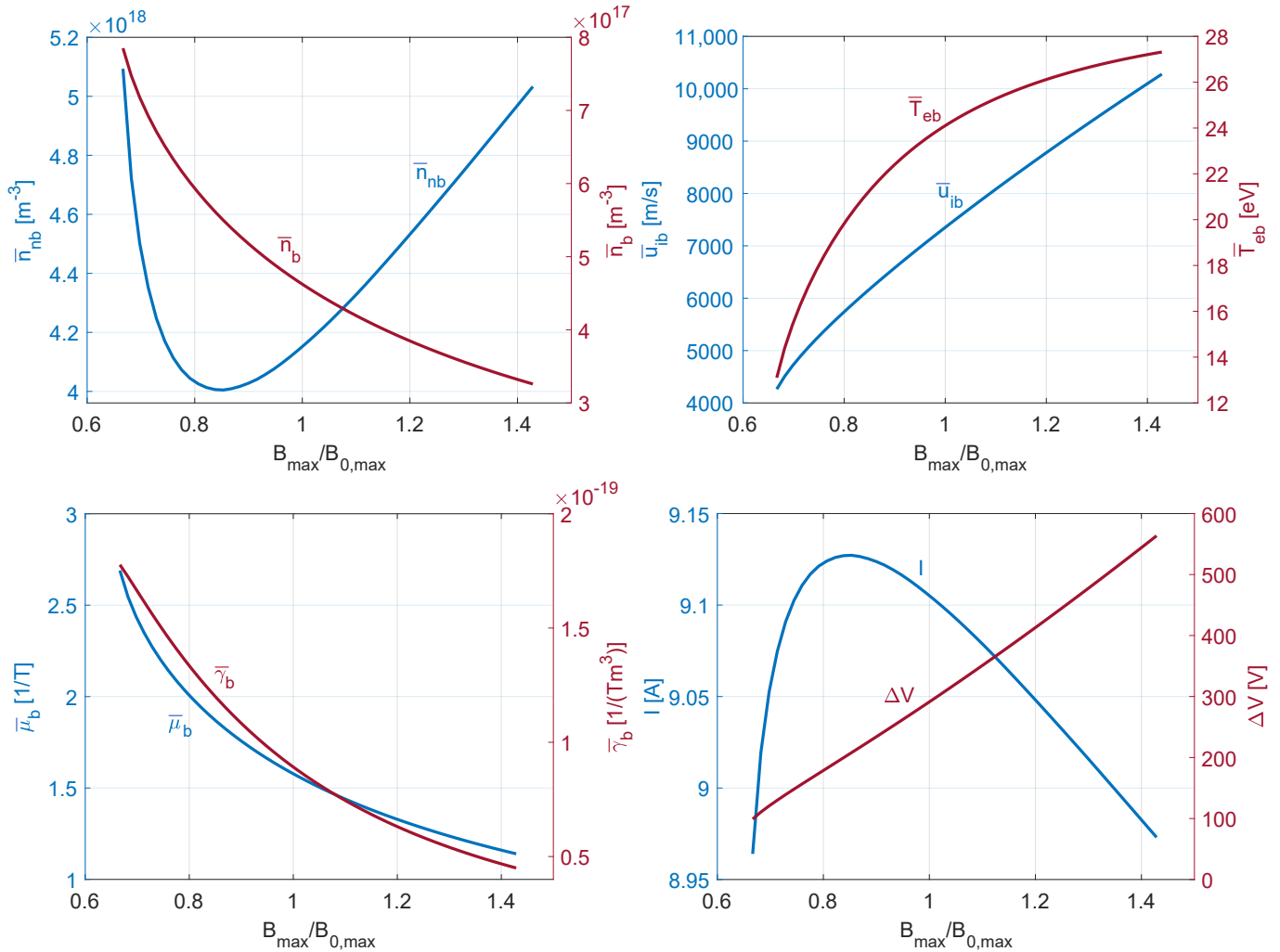


**Figure 4.** Steady-state solution of the model for varying magnetic field intensity: neutral and plasma densities (top-left), ion velocity and electron temperature (top-right), mobility and rigidity coefficient (bottom-left), and discharge current and potential drop within the channel (bottom-right).

The resulting plasma density is determined by a balance between plasma generation due to ionization and ion convection outside of the channel due to the electric field. The fact that  $\bar{n}_b$  decreases for increasing  $B_{max}$  seems to indicate that the latter mechanism is dominant. The neutral density, instead, presents a non-monotonic behavior because, on one side, the ionization rate increases with the magnetic field, while on the other side, the plasma density is lowered.

The discharge current displays little sensitivity to fluctuations in the magnetic field, exhibiting small variations with a peak occurring at low magnetic field intensities.

The potential drop within the thruster channel,  $\Delta V = \bar{E} L_{ch}$ , is an output of the model and can be computed by considering that  $\frac{1}{V} \int_V n E dV = c_{17} \bar{n} \bar{E} = c_8 \bar{n} \frac{\bar{u}_i}{\bar{\mu}}$ , where from the comparison with the 1D calibrated solution,  $c_{17} = 0.73$ . Thus, the average electric field within the channel can be approximated as  $\bar{E} = \frac{c_8}{c_{17}} \frac{\bar{u}_i}{\bar{\mu}}$ . As expected,  $\Delta V$  increases with the intensity of the magnetic field, due to the higher resistivity within the channel. This is the main difference compared to previous 0D formulations, such as the one of Hara et al. [18], where it was assumed that the whole discharge voltage was applied between the anode and the thruster exit section, and thus, the electric field was fixed and constant in time. Note that the potential drop can exceed 300V, which is the discharge voltage for the

operating condition of reference. This is a consequence of the fact that a variation in the operating conditions (in this case, the magnetic field strength) would require the 1D reference condition to be re-calibrated by varying the free parameters ( $u_n, \alpha, \beta$ ), resulting in different values of both the coefficients reported in Table 1 and the plasma parameters at the base state. Finally, Figure 4 shows that the rigidity coefficient  $\bar{\gamma}$ , as well as the electron mobility, decreases monotonically with  $B_{max}$ . It is possible to explain this behavior by looking at Equation (17): since  $\omega_e \gg \nu_{eb}$ , then  $\gamma \propto \frac{1}{\omega_e^2}$ , which decreases with the magnetic field to the second power. This is the reason why, at least in the present model, the breathing mode is suppressed when the strength of the magnetic field is enhanced.

### 3.2. Effect of Propellant and Anode Temperature

In order to investigate how the use of different propellants can affect the thruster's stability, we expanded the model's reaction database to account for krypton and argon. The reaction rates for the new propellants ( $k_I(\bar{T}_e)$ ,  $K(\bar{T}_e)$ ) are again derived from the Biagi database [29] by using the Bolsig+ [30] solver. Table 2 reports the atomic mass and ionization energy of each propellant.

**Table 2.** Atomic mass and ionization energy for xenon, krypton, and argon.

Propellant	Atomic Mass	Ionization Energy (eV)
Xenon	131.3	12.13
Krypton	83.8	13.99
Argon	39.95	15.76

As a first approximation, we consider the 0D model tuned with the same value of the coefficients reported in Table 1. The propellant mass flow rate is also the same as in the previous section, as well as the values of  $\alpha$  and  $\beta$ . We highlight that, since we considered the thruster to operate at the same mass flow rate for each of the propellants under investigation, the resulting operating power is different.

Figure 5 compares the results of the linear stability analysis for xenon, krypton, and argon. Each propellant exhibits a similar behavior, with the growth rate and frequency, respectively, decreasing and increasing monotonically with the magnetic field intensity. For most of the considered range of  $B_{max}$ , the use of krypton and argon resulted in higher growth rates compared to xenon. Krypton, however, shows a more gradual increase at low magnetic fields, and the transition value is approximately coincident with that observed for xenon. Argon, instead, clearly shows a larger growth rate compared to the other two propellants for the same  $B_{max}$ , with a transition point at stronger magnetic fields. Overall, these results suggest that the thruster tends to lose stability more easily when operating with lighter propellants.

Regarding the frequency, xenon and krypton again display comparable trends, with krypton consistently showing higher values than xenon. Argon seems to be more susceptible to variations in the magnetic field, especially at lower values, where the curve is steeper. In general, the results seem to indicate that the lighter the propellant, the higher the frequency tends to be, even though the displayed trend is not univocal at low magnetic fields.

These results are again coherent with the proposed physical interpretation of the breathing mode: the lighter the propellant, the lower the inertia of the ions, which are more susceptible to variations in the electric field in response to variations in neutral density. As a consequence, the feedback mechanism is stronger, and the time needed to empty and refill the chamber is lower, resulting in stronger and more frequent plasma surges.

Lastly, we employed the tuned model to investigate the effect of the anode temperature on the thruster stability. Figure 6 displays the growth rate and frequency for each of the propellants under investigation for an anode temperature ranging from 300 K to 900 K. In general, higher anode temperatures correspond to lower growth rates and frequencies, independently of the propellants. The stability threshold is shifted towards lower values,

especially for argon, which is the lightest of the propellants considered in this study. Ultimately, these results indicate that increasing the anode temperature has a beneficial effect on the thruster’s stability. A similar implication was also suggested in [35], where the authors showed that decreasing the residence time of neutrals can improve the thruster’s stability. These results seem to suggest that, during the initial phase after ignition, the thruster is more susceptible to the onset of breathing mode oscillations, while it tends to stabilize after the thermal transient when the anode is hot.

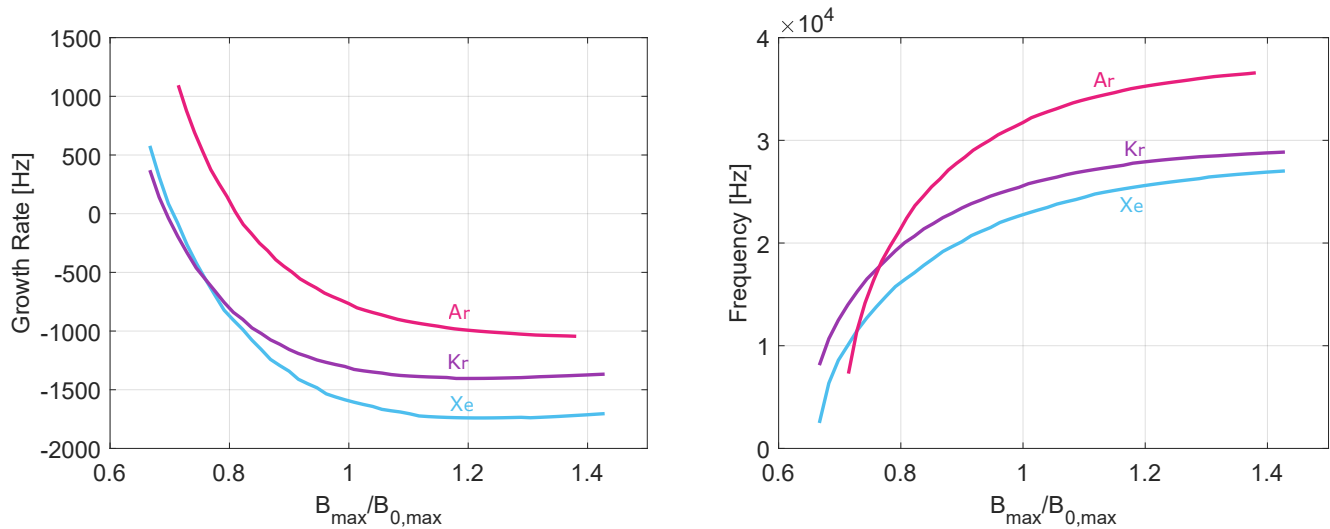


**Figure 5.** Growth rate (left) and frequency (right) of the dominant mode resulting from the linear stability analysis applied to the tuned equations, under varying magnetic field intensity: comparison between xenon, krypton, and argon.

Finally, it is worth highlighting again the role of the rigidity coefficient in the onset of the instability. Figure 7 displays the growth rate and frequency of the dominant eigenvalue for varying  $B_{max}$  when  $\bar{\gamma}$  is artificially increased by a factor of  $k$ . It is shown that increasing  $\bar{\gamma}$  artificially leads to consistently higher growth rates, shifting the transition to higher values of the magnetic field and confirming its key role in the onset of the instability.

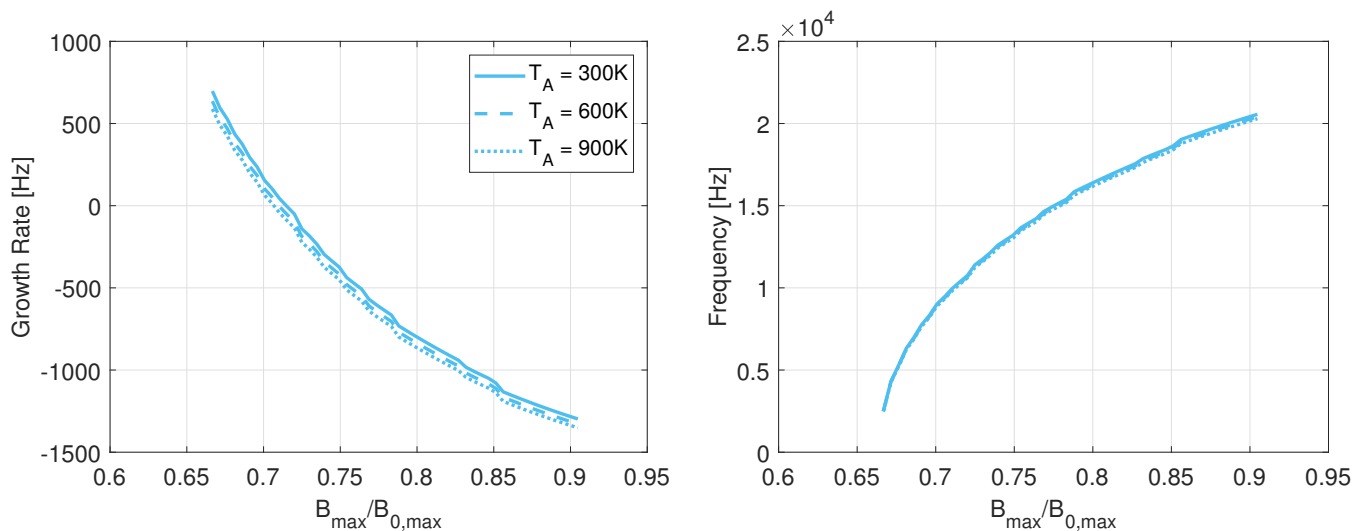


**Figure 6.** Cont.

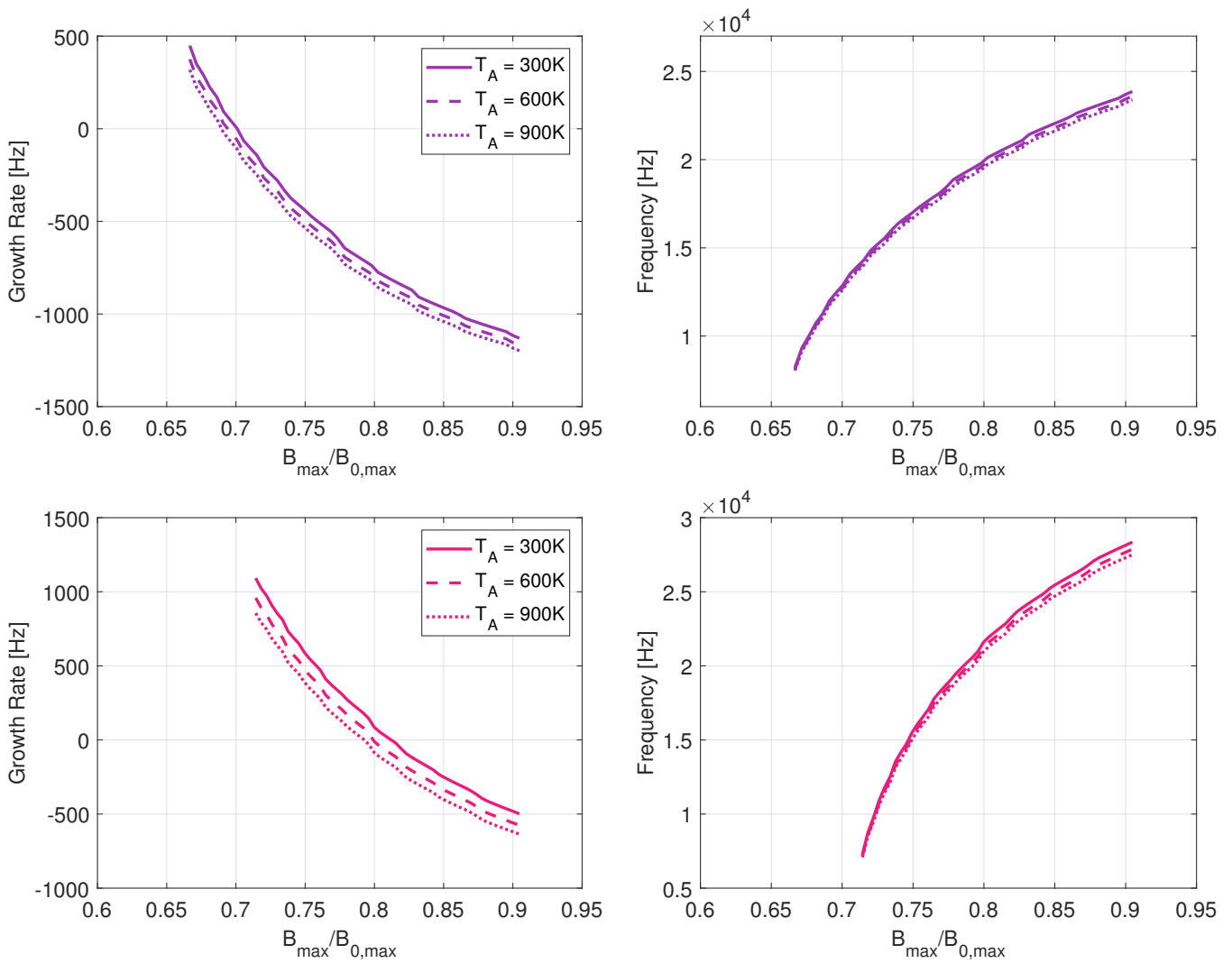


**Figure 6.** Effect of the anode temperature on the growth rate (left) and frequency (right) for xenon (top), krypton (middle), and argon (bottom).

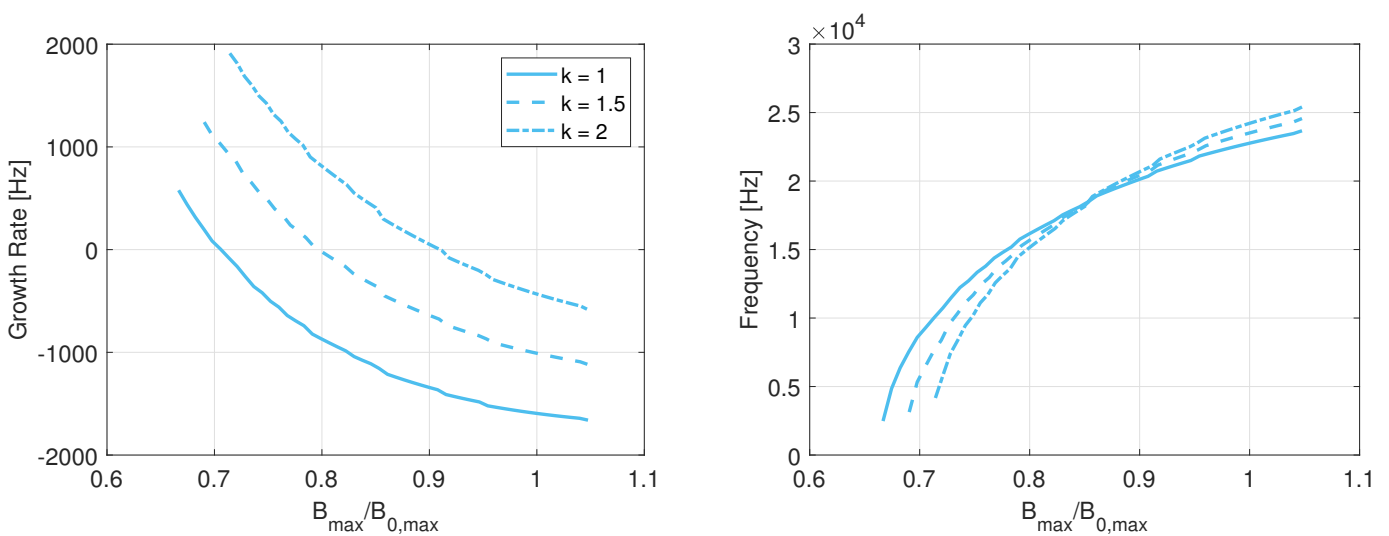


**Figure 7.** Growth rate (left) and frequency (right) of the dominant mode resulting from the linear stability analysis when  $\bar{\gamma}$  is artificially modulated by a factor of  $k$ . The transition point is shifted toward higher magnetic field intensities when  $\bar{\gamma}$  is increased.

#### 4. Conclusions

In this paper, we have investigated the effect of several operating parameters on the thruster's stability by using the 0D model of the discharge developed and characterized in [20]. To carry this out, we have introduced a closure for the average mobility and rigidity coefficient, which are related to the magnetic field strength within the thruster channel. The results of the linear stability analysis for varying magnetic field intensities yielded only stable solutions but frequencies comparable to the experimental observations. We argued that a possible reason for the lack of unstable results was that the approximations made in the model derivation were not fully representative of the system behavior. Thus, to obtain a more representative formulation of the thruster discharge, we relaxed the model assumptions by introducing a set of constant coefficients in the model equations. The coefficients were calculated by comparing term-by-term the 0D equations with the 1D formulation from which they were derived and taking the base state associated with the 1D experimentally calibrated solution as a reference state. The linear stability analysis applied to the tuned model showed a decreasing trend for the growth rate for increasing magnetic field intensity. Interestingly, the system exhibited a stability threshold at low magnetic fields, below which the growth rate becomes positive and the system loses stability. This behavior was coherent with the local-to-global mode transition typically observed in experiments from other authors and with other thrusters. Nevertheless, a discrepancy between the values of the growth rate of the 0D and the 1D model was observed for the same value of the magnetic field, indicating that localized plasma behavior could play an important role in the onset and development of the instability.

The tuned model was then employed to simulate the behavior of the thruster with the same mass flow rate of different propellants, namely, krypton and argon. Overall, the results suggest that the lighter the propellant, the more unstable the system tends to be, and the larger the frequency of the oscillations. Finally, we analyzed the effect of the anode temperature, showing that an increase in this parameter could have beneficial effects on the thruster stability, especially for lighter propellants.

In conclusion, in this work we presented a numerical framework that further demonstrates, contrary to prior beliefs, that breathing mode in Hall thrusters can be reproduced by pure 0D formulations. Moreover, the presented results indicate how the magnetic field intensity and the type of propellant affect the development of the instability. The proposed 0D formulation incorporated insight from higher-order 1D simulations calibrated on experimental data for a reference condition, and it was employed to extrapolate the main trends in discharge stability when moving away from the calibrated operating point. In the absence of a wider dedicated set of experimental data to perform a direct comparison of the results, they were discussed in light of the existing literature. The general trends reproduced by the proposed formulation agree well with previous experimental observations, such as the local-to-global mode transition for low magnetic field intensities. These works considered different thrusters and operating conditions, so they are not suitable for a direct comparison with our results. However, the fact that similar trends were observed for different configurations seems to indicate that this behavior represents a general feature of Hall thrusters, which our simplified model was able to reproduce. We acknowledge, however, that the results of the present numerical study would greatly benefit from a direct quantitative comparison with dedicated experiments, which is a future activity that we are planning to perform.

**Author Contributions:** Conceptualization, L.L., T.A. and V.G.; methodology, L.L., T.A. and V.G.; software, L.L. and F.Y.; validation, L.L.; formal analysis, L.L. and F.Y.; investigation, L.L., F.Y., T.A. and V.G.; resources, T.A.; writing—original draft preparation, L.L. and F.Y.; writing—review and editing, T.A. and V.G.; visualization, L.L. and F.Y.; supervision, T.A. and V.G. All authors have read and agreed to the published version of the manuscript.

**Funding:** This research received no external funding

**Data Availability Statement:** The raw data supporting the conclusions of this article will be made available by the authors on request.

**Acknowledgments:** The authors would like to thank Simone Camarri for the fruitful discussion.

**Conflicts of Interest:** The authors declare no conflict of interest.

## References

1. Jahn, R.G. *Physics of Electric Propulsion*; McGraw-Hill: New York, NY, USA, 1968.
2. Goebel, D.M.; Katz, I. *Fundamentals of Electric Propulsion: Ion and Hall Thrusters*; Wiley: Hoboken, NJ, USA, 2008. [[CrossRef](#)]
3. Boeuf, J.P. Tutorial: Physics and modeling of Hall thrusters. *J. Appl. Phys.* **2017**, *121*, 011101. [[CrossRef](#)]
4. Choueiri, E.Y. Plasma oscillations in Hall thrusters. *Phys. Plasmas* **2001**, *8*, 1411–1426. [[CrossRef](#)]
5. Tilinin, G.N. High-frequency plasma waves in a Hall accelerator with an extended acceleration zone. *Sov. Phys. Tech. Phys.* **1977**, *22*, 974–978.
6. Sekerak, M.J.; Gallimore, A.D.; Brown, D.L.; Hofer, R.R.; Polk, J.E. Mode Transitions in Hall-Effect Thrusters Induced by Variable Magnetic Field Strength. *J. Propuls. Power* **2016**, *32*, 903–917. [[CrossRef](#)]
7. Sekerak, M.J.; Longmier, B.; Gallimore, A.; Huang, W.; Kamhawi, H.; Hofer, R.R.; Jorns, B.; Polk, J.E. Mode Transitions in Magnetically Shielded Hall Effect Thrusters. In Proceedings of the 50th AIAA/ASME/SAE/ASEE Joint Propulsion Conference, Cleveland, OH, USA, 28–30 July 2014. [[CrossRef](#)]
8. Giannetti, V.; Piragino, A.; Paissoni, C.A.; Ferrato, E.; Estublier, D.; Andreussi, T. Experimental scaling laws for the discharge oscillations and performance of Hall thrusters. *J. Appl. Phys.* **2022**, *131*, 013304. [[CrossRef](#)]
9. Lobbia, R.; Gallimore, A. A Method of Measuring Transient Plume Properties. In Proceedings of the 44th AIAA/ASME/SAE/ASEE Joint Propulsion Conference & Exhibit, Hartford, CT, USA, 21–23 July 2008. [[CrossRef](#)]
10. Lobbia, R.B.; Gallimore, A.D. High-speed dual Langmuir probe. *Rev. Sci. Instrum.* **2010**, *81*, 073503. [[CrossRef](#)] [[PubMed](#)]
11. Giannetti, V.; Saravia, M.M.; Andreussi, T. Measurement of the breathing mode oscillations in Hall thruster plasmas with a fast-diving triple Langmuir probe. *Phys. Plasmas* **2020**, *27*, 123502. [[CrossRef](#)]
12. Fabris, A.L.; Young, C.V.; Cappelli, M.A. Time-resolved laser-induced fluorescence measurement of ion and neutral dynamics in a Hall thruster during ionization oscillations. *J. Appl. Phys.* **2015**, *118*, 233301. [[CrossRef](#)]
13. Mazouffre, S. Laser-induced fluorescence diagnostics of the cross-field discharge of Hall thrusters. *Plasma Sources Sci. Technol.* **2012**, *22*, 013001. [[CrossRef](#)]
14. Dale, E.T.; Jorns, B.A. Non-invasive time-resolved measurements of anomalous collision frequency in a Hall thruster. *Phys. Plasmas* **2019**, *26*, 013516. [[CrossRef](#)]
15. Chaplin, V.H.; Lobbia, R.B.; Lopez Ortega, A.; Mikellides, I.G.; Hofer, R.R.; Polk, J.E.; Friss, A.J. Time-resolved ion velocity measurements in a high-power Hall thruster using laser-induced fluorescence with transfer function averaging. *Appl. Phys. Lett.* **2020**, *116*, 234107. [[CrossRef](#)]
16. Fife, J.; Martinez-Sanchez, M.; Szabo, J. A Numerical Study of Low-Frequency Discharge Oscillations in Hall Thrusters. In Proceedings of the 33rd Joint Propulsion Conference and Exhibit, Seattle, WA, USA, 6–9 July 1997. [[CrossRef](#)]
17. Boeuf, J.P.; Garrigues, L. Low frequency oscillations in a stationary plasma thruster. *J. Appl. Phys.* **1998**, *84*, 3541–3554. [[CrossRef](#)]
18. Hara, K.; Sekerak, M.J.; Boyd, I.D.; Gallimore, A.D. Perturbation analysis of ionization oscillations in Hall effect thrusters. *Phys. Plasmas* **2014**, *21*, 122103. [[CrossRef](#)]
19. Dale, T.; Jorns, B.A. Two-zone Hall thruster breathing mode mechanism, Part I: Theory. In Proceedings of the 36th International Electric Propulsion Conference, IEPC-2019-354, Vienna, Austria, 15–20 September 2019.
20. Leporini, L.; Giannetti, V.; Camarri, S.; Andreussi, T. An unstable OD model of ionization oscillations in Hall thruster plasmas. *Front. Phys.* **2023**, *10*, 1097813. [[CrossRef](#)]
21. Barral, S.; Ahedo, E. Theoretical Study of the Breathing Mode in Hall Thrusters. In Proceedings of the 42nd AIAA/ASME/SAE/ASEE Joint Propulsion Conference & Exhibit, Sacramento, CA, USA, 9–12 July 2006; Volume 10, p. 5172. [[CrossRef](#)]
22. Barral, S.; Ahedo, E. Low-frequency model of breathing oscillations in Hall discharges. *Phys. Rev. E* **2009**, *79*, 046401. [[CrossRef](#)]
23. Hara, K.; Sekerak, M.J.; Boyd, I.D.; Gallimore, A.D. Mode transition of a Hall thruster discharge plasma. *J. Appl. Phys.* **2014**, *115*, 203304. [[CrossRef](#)]
24. Hara, K.; Mikellides, I.G. Characterization of low frequency ionization oscillations in Hall thrusters using a one-dimensional fluid model. In Proceedings of the 2018 Joint Propulsion Conference, Cincinnati, OH, USA, 9–11 July 2018. [[CrossRef](#)]
25. Leporini, L.; Giannetti, V.; Saravia, M.M.; Califano, F.; Camarri, S.; Andreussi, T. On the onset of breathing mode in Hall thrusters and the role of electron mobility fluctuations. *Front. Phys.* **2022**, *10*, 951960. [[CrossRef](#)]
26. Lafleur, T.; Chabert, P.; Bourdon, A. The origin of the breathing mode in Hall thrusters and its stabilization. *J. Appl. Phys.* **2021**, *130*, 053305. [[CrossRef](#)]
27. Chapurin, O.; Smolyakov, A.I.; Hagelaar, G.; Boeuf, J.P.; Raitses, Y. Fluid and hybrid simulations of the ionization instabilities in Hall thruster. *J. Appl. Phys.* **2022**, *132*, 053301. [[CrossRef](#)]
28. Giannetti, V.; Saravia, M.M.; Leporini, L.; Camarri, S.; Andreussi, T. Numerical and Experimental Investigation of Longitudinal Oscillations in Hall Thrusters. *Aerospace* **2021**, *8*, 148. [[CrossRef](#)]
29. Biagi, S. Biagi Database. Available online: [www.lxcat.net](http://www.lxcat.net) (accessed on 9 March 2021).

30. Hagelaar, G.J.M.; Pitchford, L.C. Solving the Boltzmann equation to obtain electron transport coefficients and rate coefficients for fluid models. *Plasma Sources Sci. Technol.* **2005**, *14*, 722. [[CrossRef](#)]
31. Hobbs, G.D.; Wesson, J.A. Heat flow through a Langmuir sheath in the presence of electron emission. *Plasma Phys.* **1967**, *9*, 85–87. [[CrossRef](#)]
32. Mettot, C.; Renac, F.; Sipp, D. Computation of eigenvalue sensitivity to base flow modifications in a discrete framework: Application to open-loop control. *J. Comput. Phys.* **2014**, *269*, 234–258. [[CrossRef](#)]
33. Sekerak, M. Plasma Oscillations and Operational Modes in Hall Effect Thrusters. Ph.D. Thesis, University of Michigan, Ann Arbor, MI, USA, 2014.
34. Ren, L.; Wang, Y.; Jin, L.; Zhou, K.; Fu, Y.; Sun, A.; Ding, W. Effect of magnetic field strength on the performance characterization of a low-power wall-less Hall thruster. *Vacuum* **2024**, *220*, 112820. [[CrossRef](#)]
35. Jorns, B.A.; Byrne, M.; Roberts, P.; Su, L.; Dale, E.; Hofer, R.R. Prediction and Mitigation of the Mode Transition in a Magnetically Shielded Hall Thruster at High-Specific Impulse and Low Power. In Proceedings of the 37th International Electric Propulsion Conference, IEPC-2022-372, Boston, MA, USA, 19–23 July 2022.

**Disclaimer/Publisher’s Note:** The statements, opinions and data contained in all publications are solely those of the individual author(s) and contributor(s) and not of MDPI and/or the editor(s). MDPI and/or the editor(s) disclaim responsibility for any injury to people or property resulting from any ideas, methods, instructions or products referred to in the content.